Accepted Manuscript

Microstructure and corrosion performance of 316L stainless steel fabricated by Selective Laser Melting and processed through high-pressure torsion

Shahir Mohd Yusuf, Mengyan Nie, Ying Chen, Shoufeng Yang, Nong Gao

PII: S0925-8388(18)32017-6

DOI: 10.1016/j.jallcom.2018.05.284

Reference: JALCOM 46260

To appear in: *Journal of Alloys and Compounds*

Received Date: 2 January 2018

Revised Date: 5 May 2018

Accepted Date: 23 May 2018

Please cite this article as: S.M. Yusuf, M. Nie, Y. Chen, S. Yang, N. Gao, Microstructure and corrosion performance of 316L stainless steel fabricated by Selective Laser Melting and processed through high-pressure torsion, *Journal of Alloys and Compounds* (2018), doi: 10.1016/j.jallcom.2018.05.284.

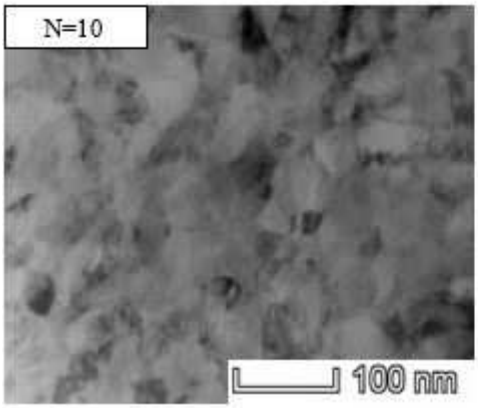

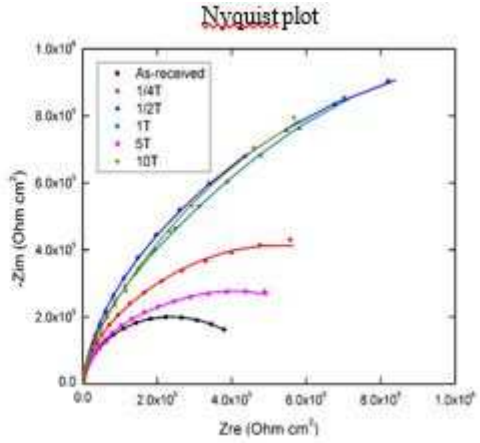

Microstructure and corrosion performance of 316L stainless steel fabricated by Selective Laser Melting and processed through High-pressure Torsion

Shahir Mohd Yusuf[a], Mengyan Nie[b], Ying Chen[c], Shoufeng Yang[a,d] and Nong Gao[a,*]

[a]Materials Research Group, Faculty of Engineering and the Environment, University of Southampton, Southampton SO17 1BJ, UK

[b]Institute for Materials Discovery, University College London, Malet Place, London WC1E 7JE, UK

[c] Fujian Provincial Key Laboratory of Functional Materials and Applications, Xiamen University of Technology, Xiamen 361024, PR China

[d]Additive Manufacturing Research Group, KU Leuven, Celestijnenlaan, 300 – box 2420 3001 Leuven, Belgium.

ABSTRACT

For the first time, the novel combination of severe plastic deformation (SPD) and Additive Manufacturing (AM) in a single process sequence was explored. 316L stainless steel (316L SS) alloy was firstly fabricated by Selective Laser Melting (SLM) AM process and subsequently processed by high-pressure torsion (HPT) SPD technique under a constant pressure of 6 GPa for different torsional revolutions. All the processed samples were subjected to electrochemical testing in a 3.5 wt % NaCl aqueous solution using open-circuit potential, potentiodynamic polarisation, and electrochemical impedance spectroscopy techniques, and characterised with scanning electron microscopy (SEM) and transmission electron microscopy (TEM). The microscopic measurement results revealed that the melt pools and cellular structures obtained via SLM become increasingly refined through increased HPT revolutions, accompanied by significant porosity reduction and significant increase in microhardness. TEM observations revealed a homogeneously distributed nano-scale grains after 10 turns. Moreover, the results demonstrated that HPT processing significantly enhances corrosion performance of the 316L SS alloy in NaCl solution, due to

the cellular structure refinement, homogeneous microstructure distribution, and the substantial removal of pores and defects. SEM and energy dispersive x-ray spectroscopy (EDX) analysis were also carried out on the corroded samples to determine the influence of cellular structure refinement on the corrosion characteristics of the 316L SS alloy.

Keywords: Selective Laser Melting, High-pressure Torsion, 316L stainless steel, Microhardness, Corrosion behaviour

* Corresponding author.

E-mail addresses: symy1g12@soton.ac.uk (S.M. Yusuf), mengyan.nie@ucl.ac.uk (M. Nie), cyj829@163.com (Y. Chen), shoufeng.yang@kuleuven.be Shoufeng Yang (S. Yang), n.gao@soton.ac.uk (N. Gao).

1. Introduction

Additive Manufacturing (AM) of metals has emerged as the sought-after manufacturing process for highly critical components which require low volume productions and mass customisation, particularly aerospace, automotive and biomedical industries. For example, turbine blades, race car components and bone implants have all been successfully fabricated by AM, with the parts having similar or even superior properties compared to those manufactured using traditional processes [1–3]. Currently, there are two classes of metal AM processes which are being widely studied including Powder Bed Fusion (PBF) and Directed Energy Deposition (DED) [4]. The PBF technique of Selective Laser Melting (SLM) is chosen as the focus of this study due to its capability of producing much finer microstructures with low porosity levels, and hence typically better mechanical and functional properties compared to its DED counterpart [5,6].

On the other hand, high-pressure torsion (HPT) is one of the severe plastic deformation (SPD) techniques that imposes significantly high strains on bulk metallic materials to achieve exceptional grain refinement, thus leading to the formation of ultra-fine grained (UFG) metallic materials which possess grain sizes < 1 μm with improved mechanical properties. To date, HPT has been widely used to produce UFG structures compared to other SPD techniques, e.g. Equal Channel Angular Pressing (ECAP) [7–9]. This is because HPT is more advantageous compared to ECAP due to its simpler operating mechanism, its effectiveness in

obtaining much smaller grains [10–12], and its capability to produce a larger amount of grain boundaries with high misorientation angles [13,14].

Of the many metals and alloys that have been the subject of various PBF AM and HPT research [15–20], 316L stainless steel (316LSS) is of particular interest because of its excellent corrosion resistance properties, which is the reason it is being widely used in applications where high level of corrosion resistance is more important than other properties, e.g. hardness and strength. At present, such applications include petrochemical industry, marine engineering, food and beverage preparing and storage, and biomedical implants. This austenitic type of stainless steel obtains its corrosion resistance characteristic via the presence of chromium (≥ 11 wt. %) which forms a thin layer of passive Cr_2O_3 oxide film on the surface of the material [21]. The addition of a small amount of molybdenum further enhances the corrosion resistance by preventing corrosion-inhibiting anions that may be present upon exposure to a corrosive environment [22]. Low carbon content (≤ 0.03 wt. %) in 316L SS is also advantageous as it could inhibit the precipitation of carbides at grain boundaries which contributes to intragranular corrosion, especially in welding process [18].

Many studies have revealed numerous factors that could influence the corrosion performance in metals and alloys, including grain sizes, corrosion media (electrolyte solution), and the surface condition of the materials, e.g. defects, surface reactivity or surface modification [22,23]. For example, Di Schino and Kenny [24] attributed the deterioration of corrosion resistance for fine-grained 304 stainless steel (grain sizes < 2 μm) in a sulfuric acid medium to the destabilisation of passive oxide layers at the grain boundaries. Li et al. [25] found that the increase in corrosion rates in nanocrystalline-grained low carbon stainless steel (grain sizes < 50 nm) produced by ultrasonic shot peening was due to the increased amounts of active sites that enhanced corrosion attacks. Another study on ECAP processing of Fe-20%Cr steel observed that the UFG structure improved the pitting resistance, and hence the corrosion resistance when immersed in a 1000 mol m^{-3} NaCl solution. On the other hand, high porosity levels and the presence of cracks have been found to contribute towards the deterioration of corrosion performance in AM-fabricated stainless steel alloy samples [26].

However, the influence of HPT processing on the corrosion resistance of SLM-fabricated 316L SS is currently unknown because these two techniques (SLM and HPT) have never been studied together. In this study, 316L SS samples were initially fabricated by SLM and

then processed through HPT. The microstructure and corrosion resistance of HPT-processed samples were investigated and compared to that of the as-received specimens. The corrosion resistance of both as-received and HPT-processed samples was carried out by conducting electrochemical tests in a sequence of open-circuit potential (OCP), electrochemical impedance spectroscopy (EIS), and potentiodynamic polarisation in a 3.5% NaCl aqueous solution.

2. Material and methods

2.1 Material and sample preparation

Gas-atomised 316L SS powder supplied by Concept Laser GmbH (CL) was used in this study. The powder particles were spherical with size distribution ranging from 5 – 55 µm, having an average particle size of ~ 25 µm (Fig. 1). The chemical composition of 316L SS powder is shown in Table 1.

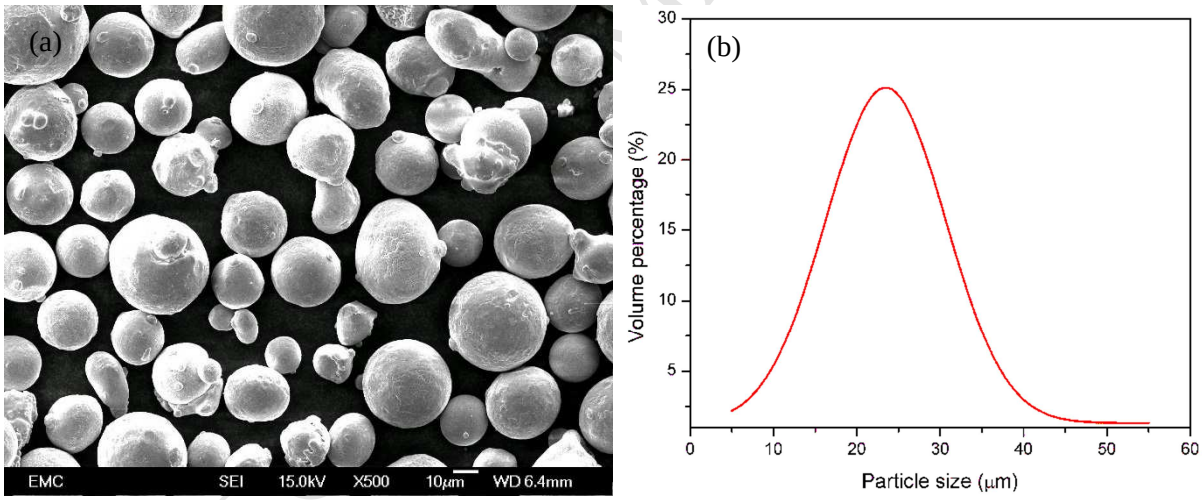

Fig. 1 316L SS powder particle morphology (a), and particle size distribution (b).

Table 1
Chemical composition of 316L SS used in this study (wt %).

	Cr	Ni	Mo	Mn	Si	P	C	S	Fe
316L SS	18.43	12.2	2.46	1.86	0.75	0.032	0.02	0.01	*Bal.*

A 200 mm long cylindrical rod with a diameter of 10 mm was manufactured using a Concept Laser M2 'Laser Cusing' Selective Laser Melting (SLM) machine. The processing

parameters of the machine used in this study are as follow: (a) laser power: 200 W, (b) scan speed: 1600 mm s^{-1}, (c) layer thickness: 30 µm, (d) scan strategy: island / checkerboard (5 x 5 mm^2). The SLM process was conducted in a protective chamber containing nitrogen gas under an operating temperature of 21°C. The build orientation of the rod was vertically upright, perpendicular to the build area (substrate).

Prior to HPT, the as-received cylindrical rod was machined to a diameter of 9.8 mm and then sliced into a series of thin disks having a thickness of ~ 1 mm before being ground with 800 grits SiC abrasive paper to a thickness in the range of 0.81 mm to 0.86 mm. Quasi-constrained HPT processing was carried out on a HPT facility at room temperature to limit material outflow from the periphery of the disk samples [27]. The facility consisted of an upper and a lower anvil containing flat, circular depressions at their centres with depth and diameter of 0.25 mm and 10 mm, respectively. The upper anvil was fixed in position, while the lower anvil moved upwards to impose compressive force and then exert torsional strain on the samples. The samples were subjected to a fixed pressure of 6 GPa under a constant rotation speed of 1 rpm in an anti-clockwise direction for 1/4, 1/2, 1, 5 and 10 turns. The equivalent strain, ε imposed by HPT can be calculated by the following equation [9]:

$$\varepsilon = \frac{2\pi NR}{h\sqrt{3}} \qquad \text{(Eqn. 1)}$$

where N is the number of turns, R is the distance from the centre, and h is the initial thickness of the sample.

2.2 Porosity, microstructural characterisation, and microhardness test

Porosity is a common defect in AM-fabricated metallic components. ImageJ analysis software was used to characterise the pores in as-received and HPT-processed 316L SS samples from the optical micrographs obtained during OM observations. 10 micrographs were used for each sample (as-received, HPT 1/4, 1/2, 1, 5, and 10 turns). Firstly, the micrographs were binarised, i.e. converted into black and white using a pre-set threshold value, in which black corresponds to porosity while white is the fabricated sample. The volume percentage (vol. %) of pores in the samples can be obtained by calculating the ratio

of black and white pixels. Surface area analysis was also carried out to determine the average pore size in the samples.

Optical microscopy (OM), scanning electron microscopy (SEM), and Transmission Electron Microscopy (TEM) were used to characterise the microstructures of the as-received and HPT-processed 316L SS samples. Prior to OM and SEM, the samples were ground using 1200 and 4000 grits SiC abrasive papers, polished using 6 µm and 1 µm diamond paste to a mirror-like surface finish. The samples were then etched using Kalling's No. 2 reagent (50 ml HCl, 50 ml ethanol, and 2g cupric chloride powder for a 100 ml solution) to reveal the microstructures of the samples. Prior to TEM, the disk samples were mechanically ground down to 80 nm and subsequently dimpled to form large thin slices using a dimple grinder (Model 656 Gatan). The thin slices were then ion-polished using PIPS II Gatan. SEM observations were conducted using JSM-JEOL 6500 FEI machine, while TEM observations were carried out using FEI Talos 200 TEM/STEM machine. The average grain size obtained after 10 turns was estimated using the intercept method [28].

Vickers microhardness (HV) tests were conducted on the as-received and HPT-processed samples using a Matsuzawa Seiki MHT-1 microhardness tester under a load of 100 gf with a dwell time of 15 s. 20 individual indentations were made at locations 3 mm from the centre of the samples and then averaged to obtain its microhardness value.

2.3 Corrosion testing

Prior to corrosion testing, the as-received and HPT-processed samples were wet ground with 1200 and 4000 grits of SiC abrasive papers, followed by polishing with 6 µm and 1 µm diamond pastes. The samples were placed inside a Teflon sample holder which served as the working electrode, in which an area of 0.28 cm^2 was exposed to the electrolyte solution. A three-electrode electrochemical cell immersed in a 3.5% NaCl electrolyte solution was used to conduct the corrosion tests with a Gamry Reference 600 potentiostat. The experiments were carried out in a Faraday cage at room temperature. A standard Ag/AgCl electrode in 3.5 M KCl solution and a graphite rod were used as reference and counter electrodes, respectively.

The samples were initially immersed in the 3.5% NaCl solution and then held for 1 hr to achieve a quasi-steady open-circuit potential. Electrochemical impedance spectroscopy was then carried out with respect to OCP with a sinusoidal AC voltage amplitude of ±10 mV over a frequency range of 100 kHz to 10 mHz. Subsequently, the potentiodynamic polarisation behaviour was determined over a range of -0.2 V to 1.5 V against OCP at a scan rate of 0.17 mV s^{-1}. All electrochemical measurements were repeated at least three times to ensure high statistical accuracy. SEM observations were then carried out on the corroded samples to compare the influence of HPT processing on the corrosion performance of SLM-fabricated 316L SS.

3. Results

3.1 Porosity, microstructure, and microhardness of HPT-processed 316L SS

Fig. 2 shows a difference in the porosity levels in the as-received and 1/4 turn HPT-processed SLM 316L SS samples. A significant decrease in porosity (91.4%) from 0.679 ± 0.051 % for the as-received sample to just 0.058 ± 0.011 % for the 1/4 HPT turn was obtained from image analysis. In addition, the average pore size decreased from 24.86 ± 18.81 µm in the as-received samples to only 4.87 ± 4.31 µm after 1/4 HPT revolutions.

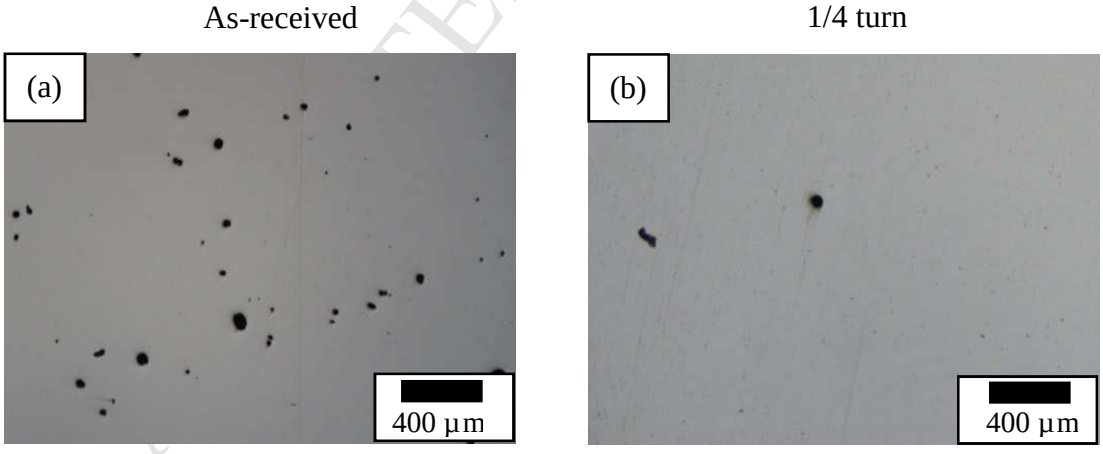

Fig. 2 Significant contrast in porosity in the as-received (a) and 1/4 turn HPT-processed (b) SLM 316L SS samples.

The results suggest that even a small number of HPT turn is capable to effectively ‘close’ the pores and dramatically reduce the size of the large pores. As shown in Fig. 3(a), a wide pore size distribution could be observed in the as-received SLM samples, ranging from 0 – 70 µm.

Most of the pores lie in the range between 10 – 40 µm. However, the pore sizes of > 50 µm initially observed in the as-received SLN sample were effectively 'closed' after 1/4 turn (Fig. 3(b)). As a result, these pores experienced immense size reduction as indicated by the higher pore count in the 0 – 5 µm range.

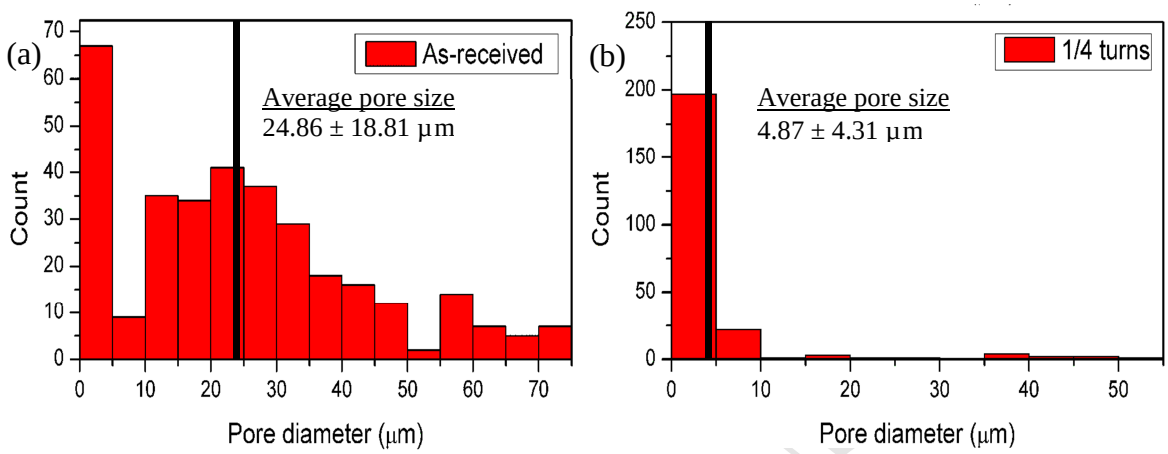

Fig. 3 Pore size distribution in as-received (a) and 1/4 HPT turn-processed (b) sample.

Fig. 4 shows the microstructures of the as-received SLM-fabricated 316L SS samples, which was observed in the x-y plane, i.e. in the scan direction. It is clear that SLM processing yielded different microstructures compared to conventional manufacturing processes; in this case, small square 'islands' representing melt pools that correspond to the 'island' scan strategy, and also cellular structures. These microstructures are similar to those obtained in previous studies by Zhong et al. [29] and Trelewicz et al. [22]. However, both studies utilised different scan strategies, and hence the melt pool structures were different than obtained in this study. Nevertheless, the cellular structures, which resemble typical welding microstructures could not be considered as actual grains as they possess low angle grain boundaries [29]. In addition, only spherical pores could be seen mainly at the edges of the small 'islands' (Fig. 4(a)), indicating that the pores were produced during powder production and not the result of the SLM process. Furthermore, non-spherical pores or cracks were not observed in the as-received SLM samples, which suggest that optimum processing parameters were used in this study.

In Fig 4(b), the laser scan direction could be observed to begin from the top towards the centre. The scan trace becomes thicker towards the end of the scan and the melt pool boundary becomes more apparent. At the highest magnification limit of OM, two distinct

microstructures are evident at each side of the melt pool boundary. Fine elongated (area A) and equiaxed (area B) cellular structures could be observed in Fig. 4(c), respectively.

SEM observations revealed a clear cellular structure with cell sizes ~ 0.5 – 1.5 µm, which is in agreement with previous studies [29], [30]. This cellular (equiaxed and rectangular bar-shape) sub-structure is formed due to the rapid, non-equilibrium heating/cooling cycle experienced during SLM (Fig. 4(d)). It was found that the cell boundaries appeared brighter compared to the cells, which might indicate enrichment by heavier elements [31]. Hence, EDX analysis was performed on the as-received SLM 316L SS sample to distinguish the elemental composition inside the cell and at the cell boundaries (area C and D inset of Fig. 4(d), respectively) and the results are displayed in Table 2.

Table 2
Chemical composition of marked areas in Fig. 4(d) in wt. %.

Area	Cr	Mn	Fe	Ni	Mo
C (inside cell)	17.90	1.90	63.69	13.84	2.67
D (cell boundary)	20.20	1.40	60.17	12.94	5.29

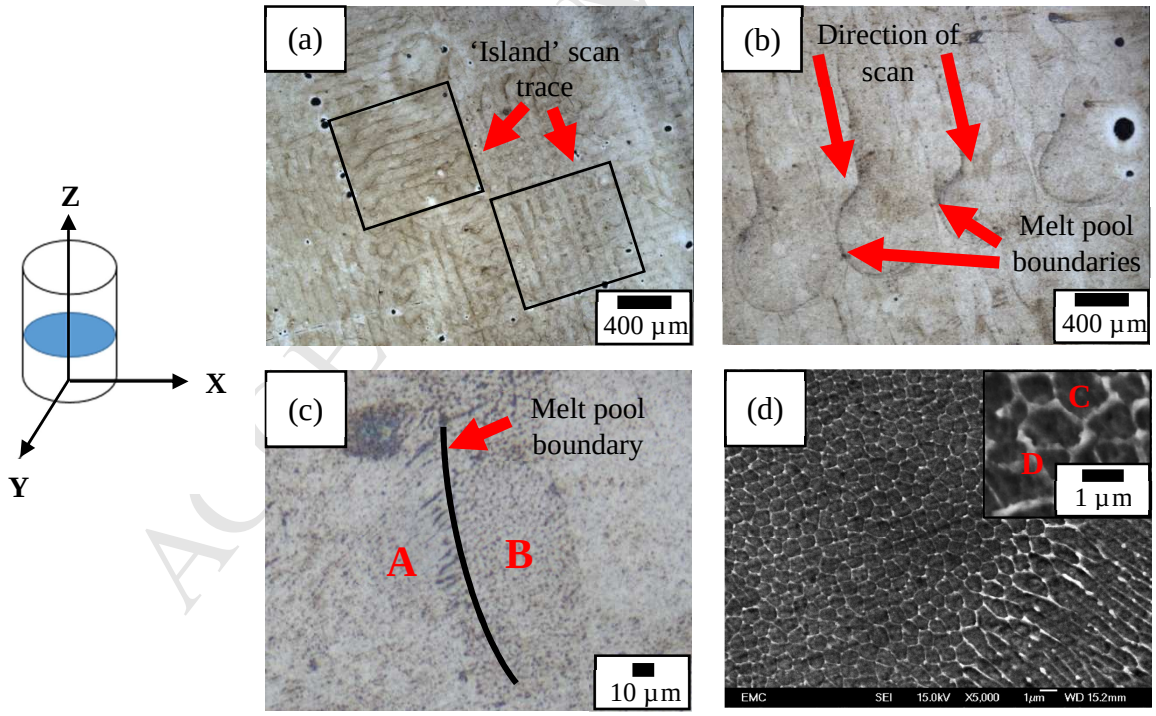

Fig. 4 As-received SLM 316L SS microstructure obtained from optical microscopy (OM). Blue indicates surface for microstructural observation (x-y plane).

Indeed, Cr and Mo enrichments with slight decrease in Ni content were observed at the cell boundaries compared to those inside the cells. The amount (wt%) of Cr, Ni, and Mo in the fabricated structure (Table 2) are higher than that of the initial powder composition (Table 1), while that of Fe is lower in the final part. Nevertheless, such elemental segregations into the cell boundaries are expected to influence the corrosion characteristics of SLM 316L SS samples [22]

Fig. 5 shows the microstructural evolution of SLM 316L SS samples processed through 1/4, 1/2, 1, 5 and 10 HPT revolutions 3 mm from the centre, obtained from OM observations. At lower number of turns (1/4, 1/2, and 1), the 'island' traces (melt pools) become increasingly elongated and disoriented as the number of turns increased, which are expected due to the increasing amount of torsional strain applied as the number of HPT turns increased. However, the melt pools became extremely distorted after 5 turns (Fig. 5(d)) before disappearing completely after 10 turns (Fig. 5(e)). This could suggest that homogeneity was reached due to the saturation in torsional strain achieved after 10 turns.

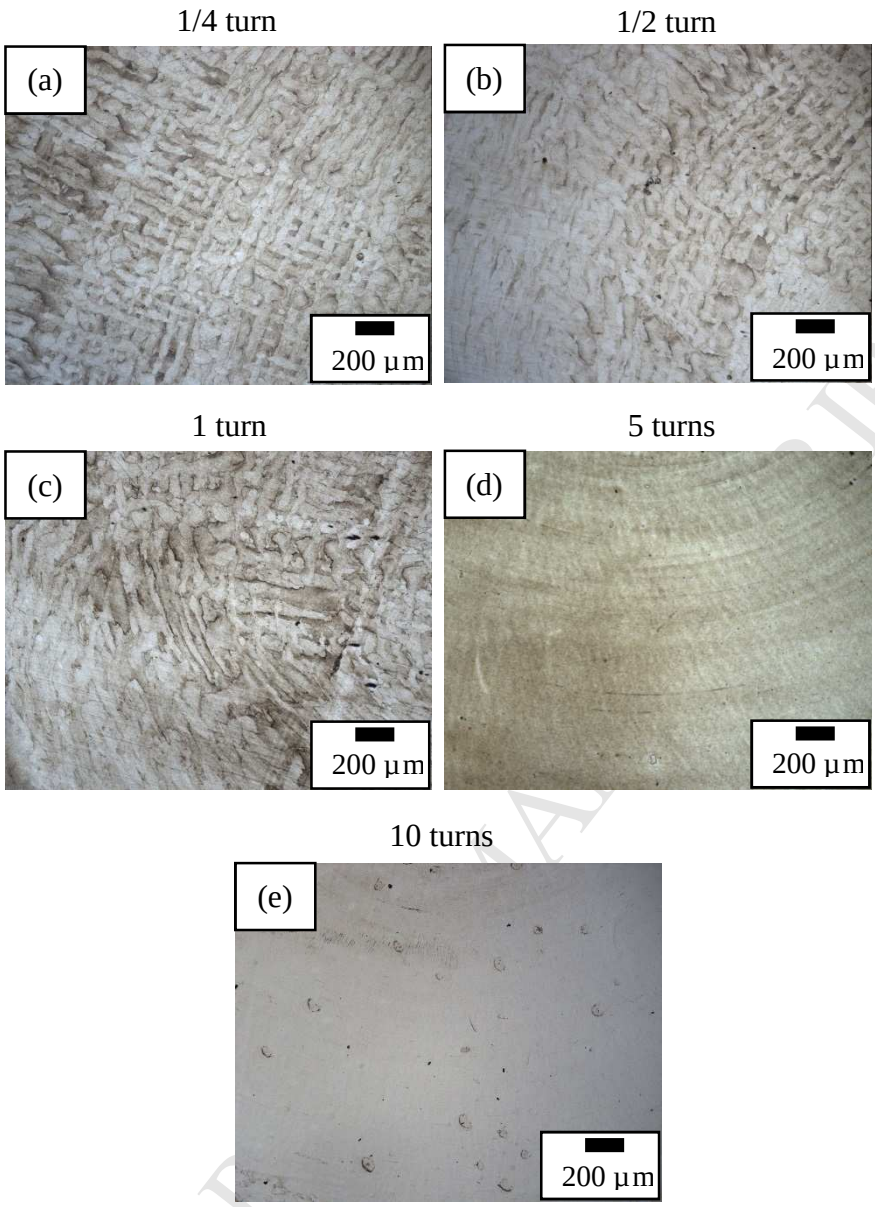

Fig. 5 Microstructural evolution of HPT-processed SLM 316L SS samples from OM.

SEM observations (3 mm from the centre) shown in Fig. 6 revealed increasing distortion of the cellular structures with higher HPT revolutions, respectively. The cells in the 1/2 turn-processed samples (Fig. 6(b)) are more lengthened and appear to rotate more than that of the samples processed through 1/4 turn (Fig. 6(a)). After 1 turn, the cells appear to be much more distorted (Fig. 6(c)). This implies that the effects of HPT processing are more apparent as the number of turns increased due to higher torsional strains in accordance with Eqn. 1.

In addition, the cellular refinement are more extreme after 5 turns , (Fig. 6(d)), which continues until 10 turns and yielded a relatively homogeneous cell distribution (Fig. 7a).

Indeed, the TEM micrograph shown in Fig. 7(b) indicates a homogeneously distributed nano-scale grains (average grain size: 33.7 ± 14.6 nm) obtained after 10 turns. In addition, the cell boundaries also become thinner as the bright areas indicating the boundaries become less apparent especially after 5 and 10 turns. These suggest that extreme refinement and elemental segregation might occur after 5 turns, which could have significant impact on the mechanical properties and corrosion resistance.

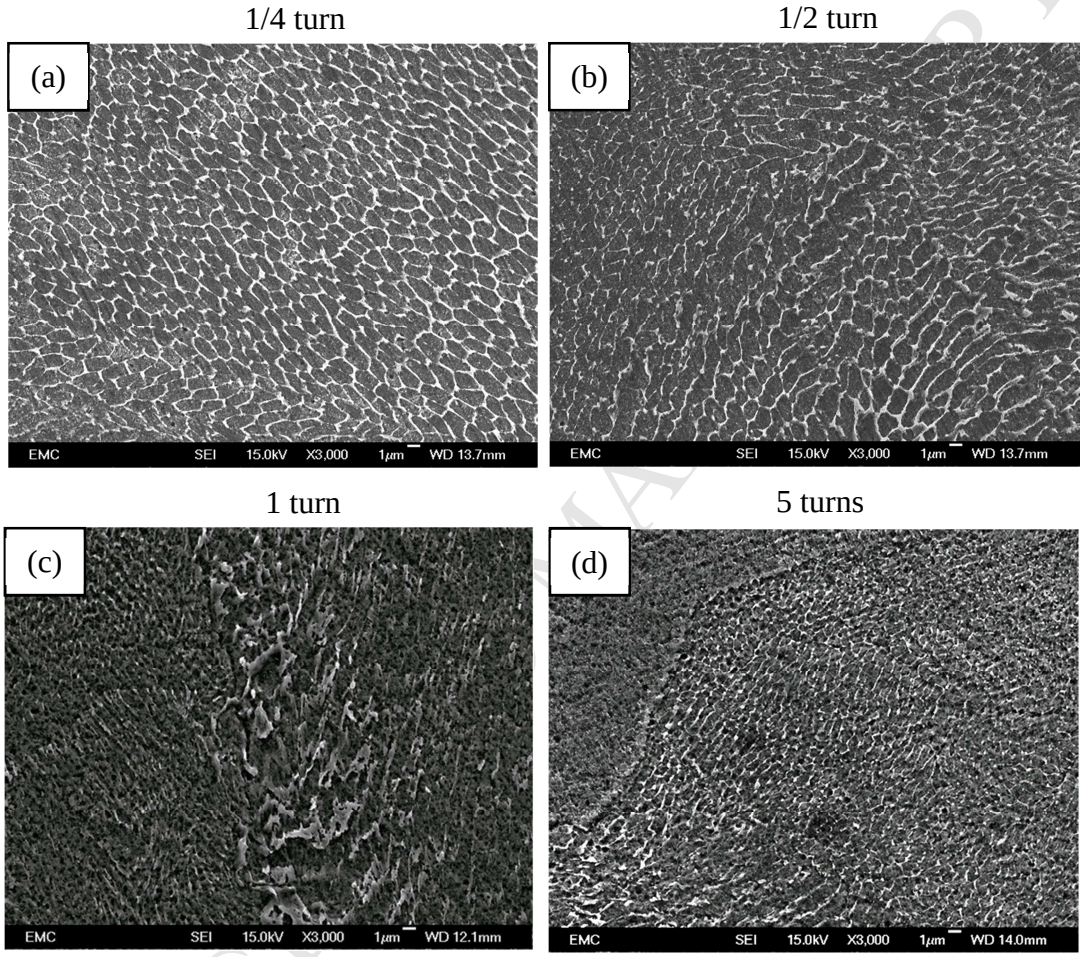

Fig. 6 Microstructural evolution of HPT-processed SLM 316L SS samples from SEM.

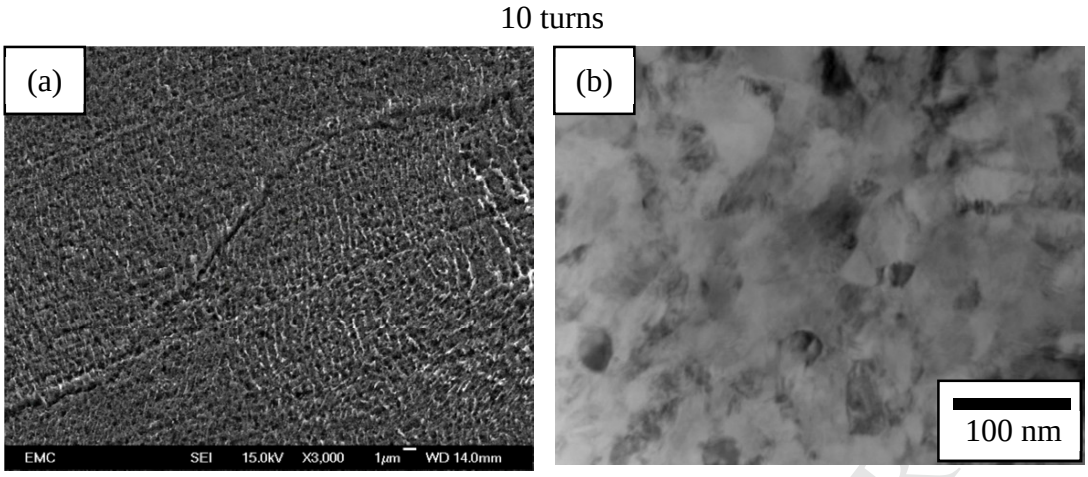

Fig. 7 SEM (a) and TEM (b) micrographs of 10-turn HPT-processed SLM 316L SS.

Fig. 8(a) displays the microhardness of the as-received and HPT-processed 316L SS samples manufactured by SLM, while Fig. 8(b) shows the corresponding strain values for each HPT revolution. HPT processing was able to significantly improve the microhardness of the SLM-fabricated samples, from 250 ± 16 HV to 346 ± 24 HV (increment of 38%) even after 1/4 revolutions only. The average microhardness values continue to rapidly increase before only improving gradually after 5 HPT revolutions. This might indicate that the microstructures become increasingly close to homogeneous distribution beyond 5 turns and peaked at 526 ± 13 HV after 10 turns. It is interesting to note that the error bars for the HV become bigger as the number of turns increase to 1/2, then become smaller up to 10 turns.

This is in good agreement with the SEM micrographs in Figs. 6 and 7(a) in which the cells are considerably smaller and more uniformly distributed beyond 1 HPT revolution. Such microstructural refinement has been reported to be attributed to large amounts of stresses and shear strains imposed due to HPT processing which results in higher dislocation densities and eventually improved microhardness values [32–34]. On the other hand, while only a gradual increment in equivalent strain values could be observed from the as-received up to 1 turn HPT-processed samples, a significant jump in equivalent strain could be observed from 1 to 5 turns and from 5 to 10 HPT revolutions (Fig. 8(b)). However, even though a substantial increase in equivalent strain was obtained upon processing through 5 and 10 turns, only a marginal increase in HV values could be observed, suggesting that a critical value leading to saturation in torsional strain and thus microstructural homogeneity is closer to be attained.

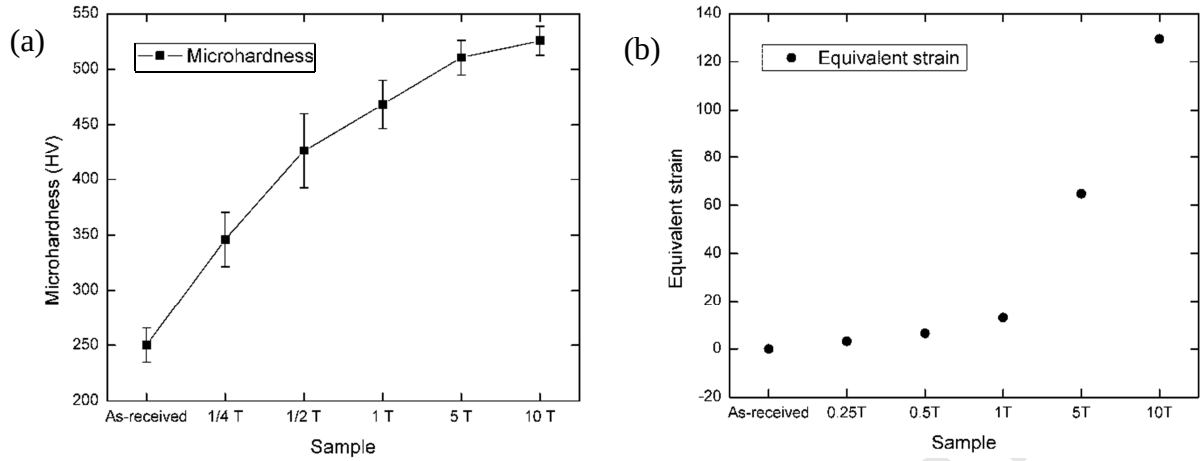

Fig. 8 Microhardness (a) and corresponding equivalent strain (b) of as-received and HPT-processed SLM-fabricated 316L SS.

3.2 Corrosion performance of HPT-processed SLM 316L SS

Electrochemical tests, including OCP, potentiodynamic polarisation, and EIS measurements, were carried out to investigate the influence of HPT processing on the corrosion performance of SLM-fabricated 316L SS samples in a 3.5 % NaCl aqueous solution.

3.2.1 Open-circuit Potential

The variation of OCP with immersion time was used as an indicator to evaluate the formation, dissolution, and stability of passive oxide layer, i.e. the corrosion tendency of the as-received and HPT-processed SLM 316L SS samples in a corrosive environment (3.5% NaCl solution). Plots of OCP against immersion time of up to 1 hr for all samples are shown in Fig. 9.

A positive shift in potential indicates the formation of a passive oxide layer on the surface of the sample, which implies a reduction in corrosion tendency and hence an improvement in corrosion resistance. On the other hand, a negative shift in potential indicates breakage or dissolution of the passive oxide layer, or even the non-existence of such protective layer. This implies increased tendency to corrosion and hence reduction in corrosion resistance. In contrast, a relatively flat curve infers simultaneous formation and dissolution of the protective oxide layer, indicating that a dynamic equilibrium has been achieved. Similarly, a steady

potential throughout immersion time means that the passive layer remains intact and protective.

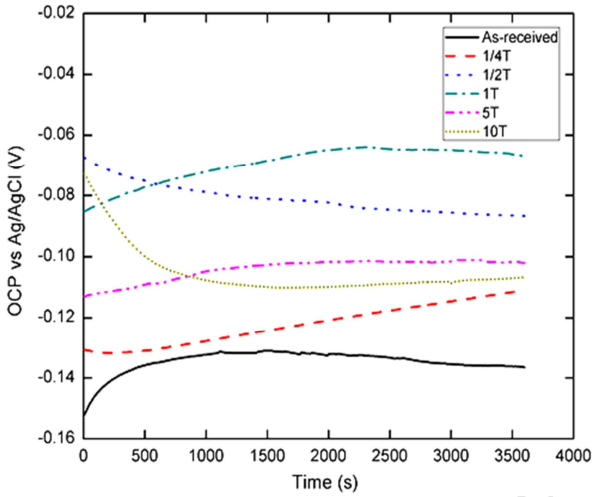

Fig. 9 OCP vs. immersion time in 3.5% NaCl solution for as-received and HPT-processed SLM 316L SS samples.

Based on Fig. 9, the OCPs for HPT-processed samples are in general more positive than that of the as-received sample, indicating that HPT processing generally improves the corrosion performance of SLM 316L SS samples in this study. Similarly, a steady-state OCP value was achieved for each sample after 1 hour immersion, indicating that a passive, protective oxide layer was formed in each case. However, within the HPT-processed samples, the corrosion tendency showed a different trend. The OCPs shift to more positive values as the number of turns increased from 1/4 to 1, exhibiting lower corrosion susceptibility and better corrosion resistance. However, upon 5 and 10 turns, the values of OCPs slightly decrease, indicating relatively greater corrosion susceptibility, but are still more positive than that of the as-received SLM sample.

Individually, the OCP for as-received sample shifts positively during the initial period of 0 s to 500 s before decreasing steadily up to 1 hour immersion. This suggests the breakage of the passive oxide layer which was formed earlier after 500 s immersion time. At 1/4 turn, a steady increase in OCP value indicates continuous formation of oxide layer throughout the test period. However, a gradual decrease of OCP value along the immersion time after 1/2 turn may indicate continuous dissolution or even absence of a passive oxide layer on the surface of the sample. After 1 and 5 turns, the OCP values exhibit improvement up to 2000 s before stabilising beyond this point, which indicate that the passive oxide layer formed

remain intact and protective. In contrast, at 10 turns, the OCP values initially decrease until ~1000 s before steadily increasing gradually, which imply that the formation of a passive oxide layer after ~1000 s could be accompanied by dissolution of the oxide layer as well. Nevertheless, all samples (as-received and HPT-processed) do not exhibit any apparent fluctuations, which suggest negligible metastable pitting were present during the corrosion process. The final OCP values for all samples and their associated errors are displayed in Table 3.

3.2.2 Potentiodynamic polarisation

Potentiodynamic polarisation test has been established as a method to quantitatively assess the corrosion performance of a material in a given environment. Fig. 10 compares the polarisation curves of as-received and HPT-processed SLM 316L SS samples through 1/4, 1/2, 1, 5, and 10 turns in the 3.5% NaCl solution at a scan rate of 0.17 mV s^{-1}. Tafel fitting analysis was carried out on the polarisation curves to determine corrosion performance parameters including corrosion potential, E_{corr}, corrosion current density, i_{corr}, corrosion rate, and pitting potential, E_{pit} [35], all of which are displayed in Table 3.

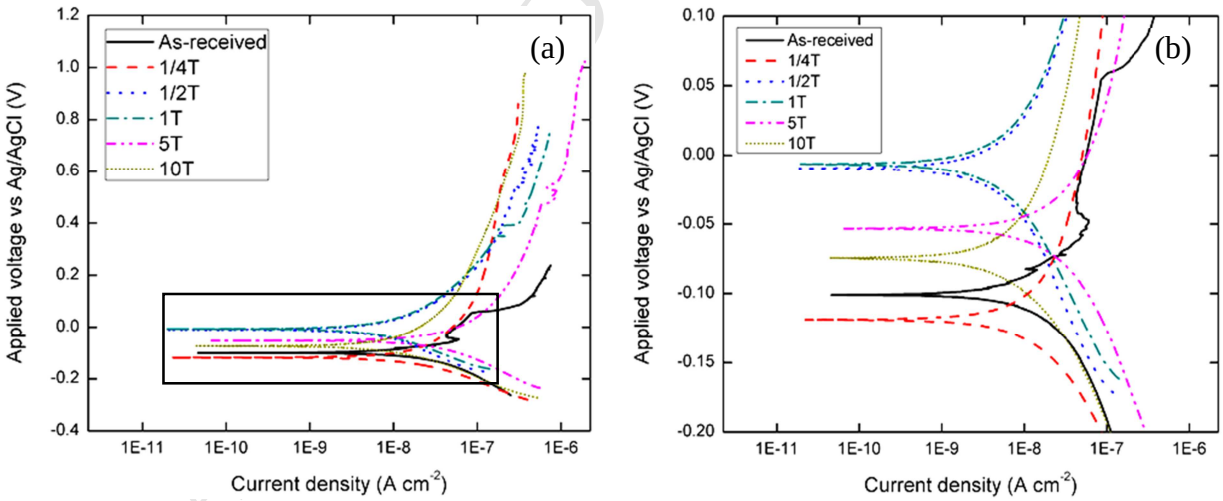

Fig. 10 Polarisation curves (a) and zoomed in view of chosen region (b) for as-received and HPT-processed SLM 316L SS samples after corrosion test.

As seen from Fig. 10 and Table 3, in general, the values of i_{corr} for HPT-processed SLM 316L SS samples are lower compared to that of the as-received sample while the values of E_{corr} of HPT-processed samples are more positive than that of the as-received, which indicate

improved corrosion performance after HPT processing. In addition, the trend of E_{corr} value with HPT processing turns is generally consistent with the results from the OCP testing. Furthermore, the reduction in corrosion rates in this study follows a similar trend as OCP with more positive values obtained with increasing HPT turns from 1/4 to 1, which indicates continuous improvement in corrosion performance at lower number of turns. Both tests indicate that 1 turn of HPT processing results in the best corrosion performance among all samples.

However, the corrosion rate after 10 turns is surprisingly lower than that after 5 turns, which is contrastingly different from the trends observed for both OCP and E_{corr} test results. Nevertheless, E_{pit} values for all HPT-processed samples are significantly greater than that for the as-received samples, suggesting that pitting corrosion becomes more difficult to occur on the HPT-processed sample surfaces as a result of further grain refinement at higher number of turns. It is noteworthy that E_{pit} values for 5 and 10 HPT turns processed samples are significantly greater than those samples processed through lower number of turns (1/4 to 1) as shown in Table 3.

Table 3
Corrosion performance of SLM 316L SS in 3.5% NaCl solution.

Sample	OCP (mV)	E_{corr} (mV)	i_{corr} (μA cm^{-2})	Corrosion rate (μm year^{-1})	E_{pit} (mV)
As-received	-136±5	-101±6	0.0616±0.0151	2.53±0.62	256±5
1/4 turn	-112±1	-108±5	0.0348±0.0078	1.43±0.32	875±8
1/2 turn	-88±4	-12±7	0.0136±0.0013	0.56±0.05	840±6
1 turn	-67±8	-7±4	0.0069±0.0051	0.41±0.01	773±9
5 turns	-103±3	-53±2	0.0521±0.0107	2.14±0.44	1028±8
10 turns	-107±1	-74±7	0.0117±0.0005	0.48±0.21	984±8

3.2.3 Electrochemical Impedance Spectroscopy

Despite OCP and potentiodynamic polarisation tests being widely used to establish the corrosion susceptibility and to determine the corrosion rates, respectively, the accuracy of the results from both tests could be compromised due to possible interference from preceding cathodic reaction on the surface of the samples [36]. Hence, electrochemical impedance spectroscopy was used to characterise the electrochemical interface between electrodes and electrolytes (3.5% NaCl solution in this study) as it is a non-destructive and sensitive

technique [37]. The properties of an electrochemical interface that are typically obtained by analysing the EIS spectra, e.g. impedance and capacitance could be used to provide further evidences for the mechanism of the corrosion process [37].

Fig. 11(a) displays the Nyquist plot, while Figs. 11(b and c) and 11(d and e) show the bode amplitude and bode phase angle plots against frequency, of the as-received and HPT-processed SLM 316L SS samples in a 3.5% NaCl solution obtained at OCP, respectively. All plots were best fitted using an equivalent circuit (EC) model having χ^2 values < 2.0 x 10^{-3} for all EIS experimental data. The EC model (inset of Fig. 10(a)) contains two time constants, representing two layers of substances in series. It consists of a solution resistance, R_u corresponding to the resistance of the 3.5% NaCl solution, two constant phase elements, CPE_{out} and CPE_{in}, and two charge transfer resistances, R_{out} and R_{in}. The first time constant corresponds to the parallel combination of R_{in} and CPE_{in} across the inner protective oxide film, while the second time constant is attributed to a parallel combination of R_{out} and CPE_{out} in the porous layer or defects on the outer surface of the samples.

In Nyquist plots (Fig. 11(a)), each curve represents a semi-circle in the low and medium frequency range, in which a large radius corresponds to a high corrosion resistance. It is clear that the HPT processing generally improves the corrosion resistance of SLM 316L SS samples as indicated by the larger curve radii compared to that of the as-received samples. In addition, samples processed through 1/2, 1 and 10 turns have greater curve radii as well as high impedance values, and hence excellent corrosion resistances compared to other samples. This observation is consistent with the aforementioned trend between the corrosion rate estimated from the potentiodynamic polarisation curves and the turns of HPT processing, thereby verified the results from both polarisation curves and EIS measurements.

Bode plot of amplitude vs. frequency in Fig. 11(b) show the impedance modulus, Z_{mod} as a function of frequency, f. Here, the polarisation resistance of the sample in the electrolyte, R_p (sum of R_{out} and R_{in}) is expressed in a low frequency limit (f < 1 Hz), R_u is expressed in a high frequency limit (f > 1 kHz), while CPE_{out} and CPE_{in} are expressed in the middle frequency (1 Hz < f < 1 kHz) [38]. It could be observed that the impedance values, i.e. R_u in the high frequency region are not influenced by the sample difference. Meanwhile, in the low frequency region, samples processed through 1/2, 1 and 10 turns have relatively higher

impedance values compared to the other samples (Fig. 11(c)). On the other hand, the middle frequency region shows a nearly linear dependence between log Z_{mod} and log f.

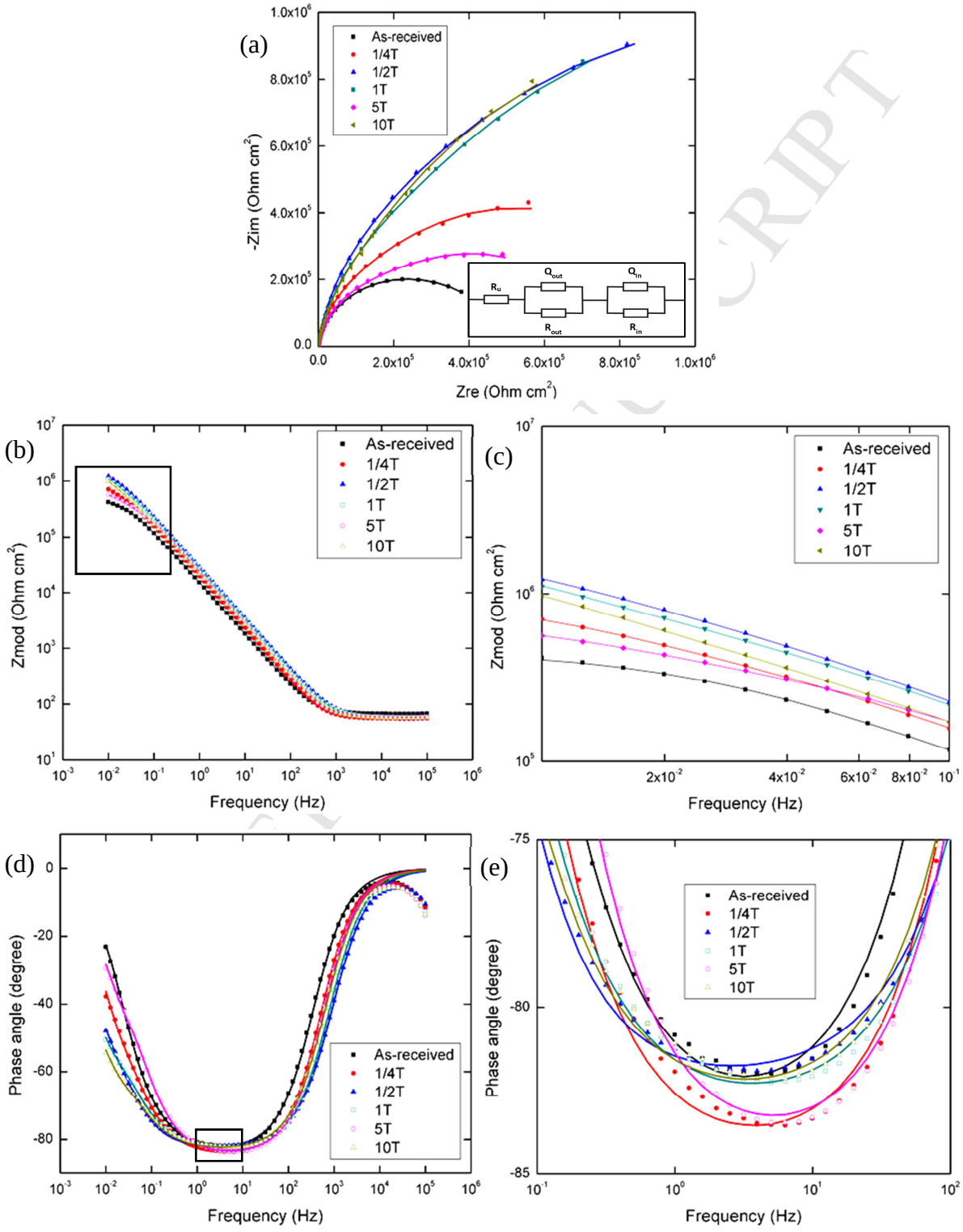

Fig. 11 Nyquist plots (a) and an equivalent circuit (inset of (a)), Bode amplitude vs. frequency plot (b) and magnified view for the low frequency region (c), Bode phase angle vs. frequency plot (d) and magnified view for the middle frequency region of phase angle plot (d) for as-received and HPT-processed SLM 316L SS samples.

Based on Bode plot of phase angle, ϕ vs frequency, f (Fig. 11(d)), the phase angles in the middle frequency region for all samples lie very closely to each other, with only a small variation between -82° to -85°. This indicates that the protective oxide layer formed primarily show a capacitive behaviour [39,40]. However, all HPT-processed samples have relatively flatter peaks compared to the as-received sample with the ϕ values extending near to 1 Hz (Fig. 11(e)). This suggests that in general, the capacitive behaviour of the HPT-processed samples could be observed over a wider range of frequency, and their protective oxide layers remain intact over a longer period of time compared to the as-received sample [41]. However, when compared among the HPT-processed samples, samples processed through 1/4 and 5 turns showed less capacitive behaviour due to their sharper peaks compared to samples processed through other number of turns.

On the other hand, CPE is essentially an element of capacitance and is used to address the non-ideal capacitive response due to surface inhomogeneity resulting from the surface roughness, impurities and grain boundaries [42–44]. The CPE impedance is defined by [37]:

$$Z_{CPE} = [Y(j\omega)^{\alpha}]^{-1} \qquad \text{Eqn. 2}$$

where Y is the admittance, defined by the ease of alternating current (AC) flow into the circuit having dimensions of Ω^{-1} cm^{-2} s^{α}, j is an imaginary number, ω is the angular frequency, and α is an exponential of the CPE determined empirically with values of $-1 \leq \alpha \leq 1$. The term α is related to the non-uniform current distribution due to the surface condition of the samples, e.g. roughness, defects, and pores. The CPE could represent a circuit parameter behaving as an ideal capacitor when α = 1, a resistor when α = 0, and an inductor when α = -1 [37]. Furthermore, the total impedance or polarisation resistance, R_p representing the overall corrosion resistance of the material in this case is obtained by adding R_{in} and R_{out}. The values for both R_{in} and R_{out} obtained from this EC model simulation are summarised in Table 4.

Table 4

Parameters of EC obtained from simulation based on the EIS experiment data.

Sample	R_u (Ω cm^2)	R_{in} (kΩ cm^2)	R_{out} (kΩ cm^2)	R_p (kΩ cm^2)	Y_{in} (10^{-4} Ω^{-1} cm^{-2} s$^{\alpha}$)	α_{in}	Y_{out} (10^{-4} Ω^{-1} cm^{-2} s$^{\alpha}$)	α_{out}
As-received	66.7±0.1	454±23	7±4	461±5	0.13±0.07	0.92±0.03	1.62±0.22	1.00±0.01
1/4 turn	55±0.1	824±18	155±16	979±1	0.16±0.03	0.93±0.05	0.20±0.04	0.93±0.04
1/2 turn	55.7±0.2	211±15	1860±102	2071±4	0.27±0.04	0.91±0.06	0.09±0.03	0.89±0.06
1 turn	58.4±0.1	160±17	2220±115	2380±7	1.12±0.04	0.91±0.03	0.15±0.02	0.97±0.03
5 turns	57.8±0.3	216±20	513±43	729±4	0.11±0.08	0.93±0.04	0.23±0.05	0.94±0.05
10 turns	56.1±0.1	351±22	1970±125	2330±9	0.17±0.02	0.93±0.02	0.16±0.03	0.98±0.02

As shown in Table 4, the polarisation resistance, R_p values of HPT-processed samples are far greater than that of the as-received sample, with a significant increase from 461 kΩ cm^2 in the as-received samples to 979 kΩ cm^2 after only 1/4 turn. This increasing trend continues until 1 revolution, before a sharp decline observed after 5 turns and a dramatic improvement after 10 turns, in which high R_p values correspond to exceptional corrosion resistance. Furthermore, after 1/4 turn, the value of R_{in} is higher than R_{out}, which suggests that the enhancement in corrosion resistance is largely contributed by R_{in}. However, as the number of turns increases, the corrosion resistance improvement is largely due to the increase in R_{out} values, as indicated by the consistently higher values of R_{out} compared to that of R_{in}.

3.3 SEM and EDX analysis

To gain further insight on the corrosion behaviour of SLM 316L SS samples through HPT processing, SEM observation and EDX analysis were conducted for the as-received and HPT-processed samples. Fig. 12 shows the surface morphology of the as-received SLM 316L SS samples before and after undergoing corrosion process, while the chemical composition at selected areas as obtained from EDX analysis is displayed in Table 5.

Table 5

Chemical composition of marked areas in Fig. 12 in wt. %.

Area	Cr	Ni	Mo	Mn	Si	S	O	Cl	Fe
E	7.84	10.31	0.67	1.02	-	-	23.72	4.53	51.91

F	12.25	10.67	1.68	3.12	-	1.44	4.05	-	66.79
G	11.23	14.38	1.12	-	10.71	-	26.33	-	50.61
H	16.55	13.07	2.65	2.04	-	-	8.53	1.14	56.02

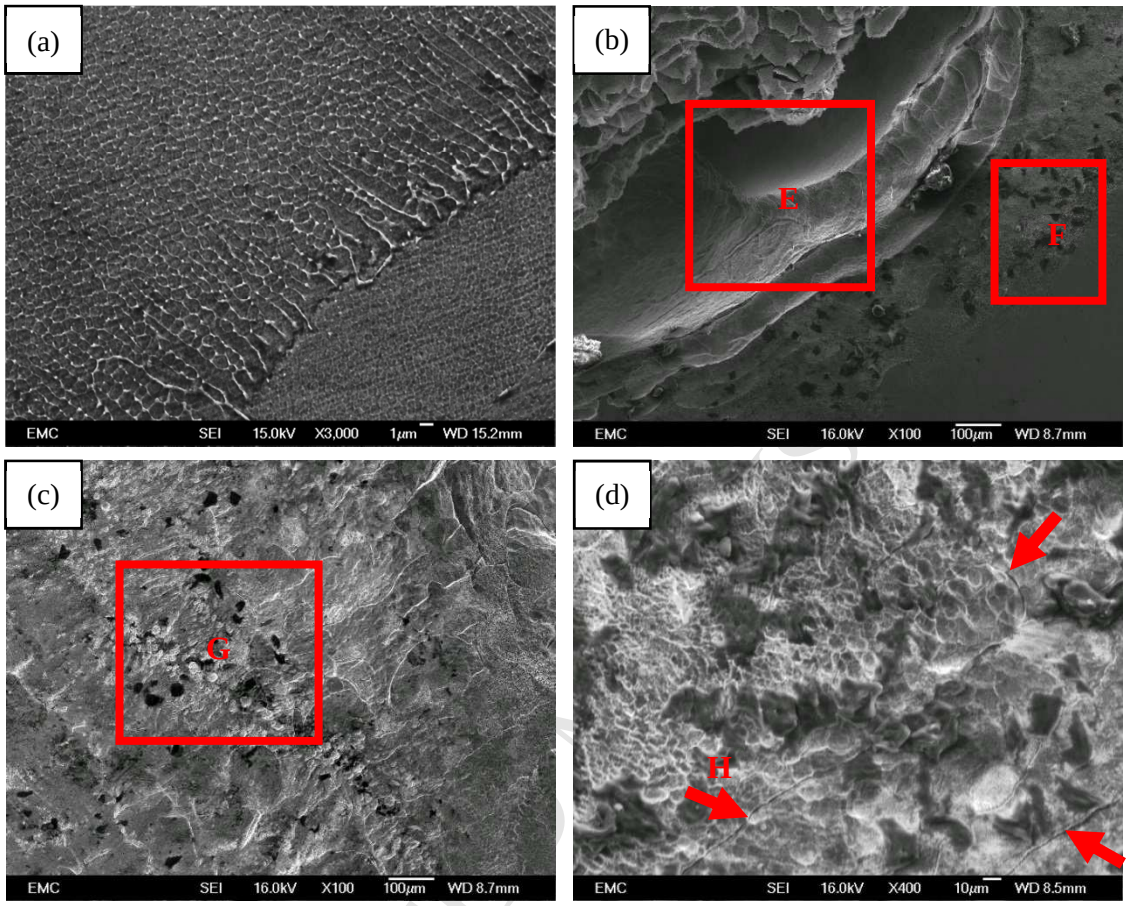

Fig. 12 Surface morphology of as-received SLM 316L SS sample before corrosion test (a) and after corrosion test (b, c, d).

A large and deep crevice could be seen formed at the periphery of the test region (Fig. 12(b)), with EDX analysis (Table 5) revealing the presence of Cl with a reduction in Cr at the crevice (area E). These suggest that the initially protective Cr_2O_3 passive layer is eventually destroyed by the attack by the Cl^- ions from the electrolyte and could not re-passivate due to the lack of oxygen [41,45]. As a result, a deep crevice was formed at the periphery of the test area. Severely corroded pits could also be observed near the crevices, suggesting that the growth of pits begin from and scatter around the crevice area (area F). The increasing amount of Mn and the emergence of S near the pits (area F) as shown in Table 5 indicate the presence of MnS inclusions which becomes one of the nucleation sites for the pits.

Moreover, surface defects such as pores could also be locations for corrosion to occur as observed in Fig. 12(c), e.g. area G. Such pores, which are typically present in SLM-fabricated samples, suffer from high metal dissolution after being exposed to the electrolyte. This is because the pores provide an easy pathway for anolyte diffusion, hence accelerating the dissolution of metal compared to other areas [46]. The presence of Si and O indicates the existence of Si-rich oxides on the surface of the pores, while Ni could also be observed to segregate to the pore area.

Upon higher magnification, corrosion attacks could be observed along the melt pool boundaries as indicated by the arrows in Fig. 12(d). This is an interesting observation as corrosion attack normally occurs along the grain boundaries, i.e. intergranular corrosion (IGC), but here the grain boundaries are poorly defined due to the fine and heterogeneous microstructure distribution as a result of SLM processing. In this case, the melt pool boundary becomes an active site for corrosion attack instead of the actual grain boundary. Hence, this type of corrosion could not be classified as IGC, but more precisely as attack along the melt pool boundaries. Results from the EDX showed slight segregation of Ni into the melt pool boundary and the presence of Cl along the attacked melt pool boundary (area H) as indicated in Table 5.

The surface morphologies of corroded HPT-processed samples through 1/4, 1/2, 1, 5 and 10 turns are shown in Fig. 13 and the elemental composition at selected areas are shown in Table 6. Crevice and pitting corrosion are common for all the HPT-processed samples with different number of turns, but the crevices are smaller and less deep compared to that of the as-received sample (Fig. 13(a), (c), (e), (g), (i)). Similarly, less pits are observed for the HPT-processed samples as the number of turns increase (red arrows). Moreover, the increase in Cr content accompanied by reduction in Fe as the number of turns increased (except for 5 turns) indicate more uniform oxide layers were formed. In addition, corrosion attack along the melt pool boundaries is also a common corrosion mechanism for the samples up until 1 turn of HPT processing.

It is noteworthy that the attack increases as the number of turns increase from 1/4 to 1/2 and breakage of the melt pool boundary is observed after 1 turn (Fig. 13(b), (d), (f)). In addition, EDX analysis also revealed an increase in the amount (wt. %) of Mn segregation into the

melt pool boundary up until 1 turn of HPT processing, suggesting that Mn played a key role in the breakage of the melt pool boundary.

Nevertheless, the overall corrosion resistance improves up to 1 turn of HPT processing based on the electrochemical tests, thus suggesting that the breakage of melt pool boundary did not significantly influence the corrosion performance compared to the crevices and pits. The significantly higher wt. % of Cr than Mn (Table 6) suggests that the formation of passive Cr_2O_3 layer outweighs the negative effect of corrosion attack at the melt pool boundary.

Beyond 1 HPT revolution, the breakage of the melt pool boundary and attack along the melt pool boundary no longer occur when observed at higher magnification, most probably due to the extreme grain refinement after 5 and 10 turns. Hence, crevice and pitting corrosion are the main corrosion mechanisms under higher number of turns HPT processing. After 5 turns, crevices corrosion attacks begin to appear again and are even larger and deeper compared to other HPT-processed samples (Fig. 13(h)). This might be the reason that samples processed through 5 turns display lower corrosion resistance compared to other HPT processed samples, despite still being performed better than the as-received sample.

EDX analysis also indicates better formation of Fe-based oxides due to the greater wt. % of Fe at 5 turns compared to at 1 and 10 turns (Table 6). However, the size and depth of these crevices decrease after 10 turns (Fig. 13(j)). Nevertheless, in both cases the amount and size of pits are much smaller compared to the as-received and HPT-processed samples at lower number of turns (1/4, 1/2, and 1) as indicated by the red arrows. The observed higher resistance to pitting corrosion is in consistence with the polarization curve measurement results of the greater E_{pit} values for the samples processed through 5 and 10 turns (Table 3).

Table 6
Chemical composition of marked areas in Fig. 12 in wt. %.

Area	Cr	Mo	Mn	O	Fe
I	15.05	-	-	29.36	55.59
J	16.25	2.61	1.44	36.42	43.28
K	16.89	2.39	1.57	41.58	36.15
L	18.27	2.23	2.04	50.70	26.76
M	14.92	2.61	1.48	49.96	31.03
N	16.77	2.65	1.45	51.26	27.87

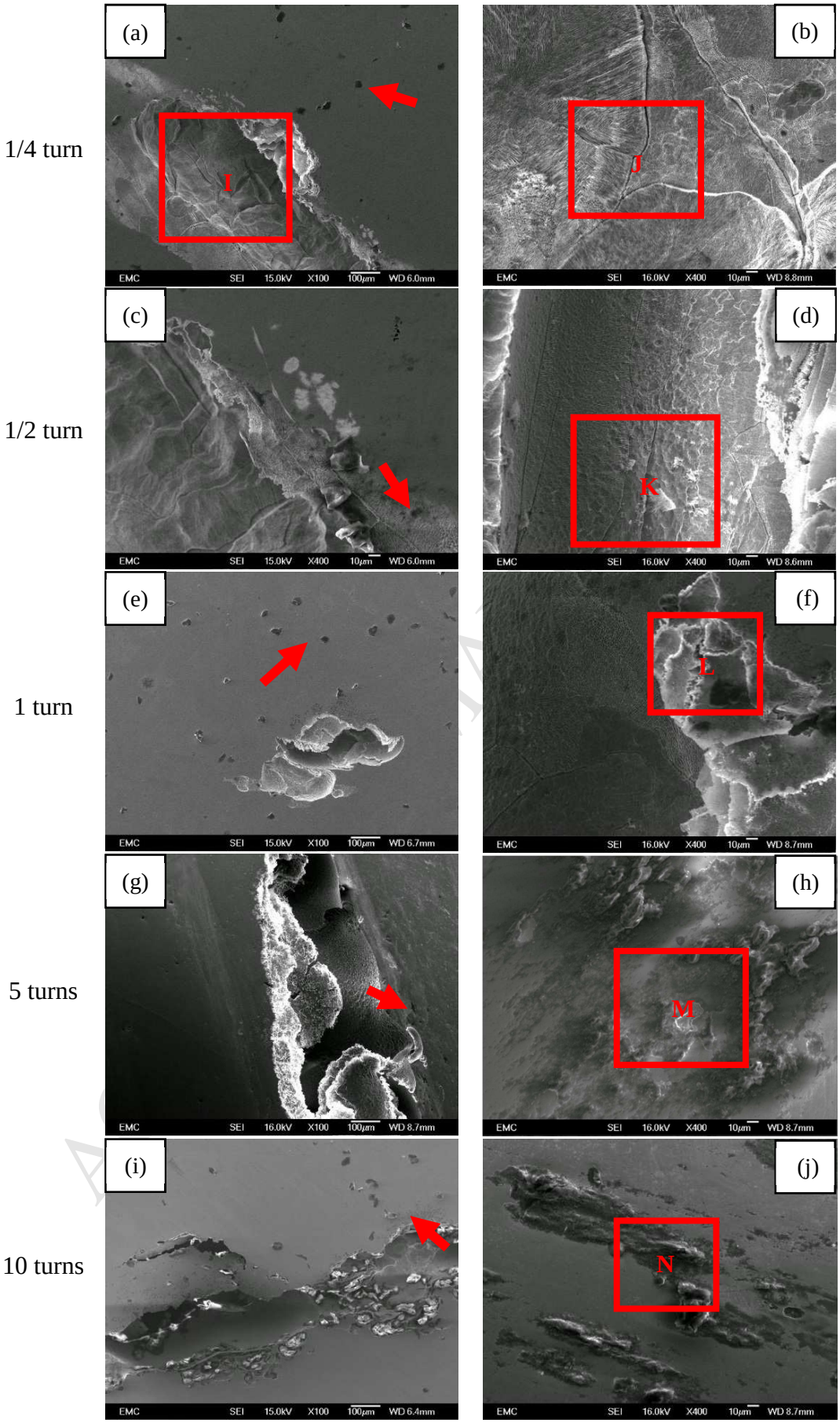

Fig 13 Surface morphology of corroded samples of SLM 316L SS processed through HPT.

4. Discussion

Metal AM processes such as SLM and EBM have often been found to produce unusual microstructures which are typically finer than their conventionally manufactured counterparts, e.g. wrought or cast. On the other hand, SPD techniques such as ECAP and HPT typically produces extreme grain refinement down to the ultrafine grained level i.e. grain sizes < 1 µm, apart from altering the grain boundary and dislocation density levels in the processed materials. In this study, the combination of SLM and HPT yielded distinct microstructures; 'island' scan traces representing the melt pools that correspond to the 'island' scan strategy, and cellular structures. Based on the OM and SEM observations, the cellular structures are heterogeneously distributed throughout the fabricated samples. However, as the number of HPT revolutions was increased, not only the cells were extremely refined, some degree of microstructural homogeneity was also introduced due to the torsional strain imposed, as indicated by the decreased error bars for the average microhardness values as the number of turns increased (Fig. 5).

In addition, the application of HPT has resulted in a significant increase in microhardness for the SLM 316L SS samples, with continuous increase in HV values as the number of turns increase, e.g. ~250 HV for the as-received SLM sample to ~525 HV after 10 turns. Such increment in HV values are attributed to the refinement of the cellular structures, reduction in porosity, as well as the introduction of dislocations due to the torsional strain imposed during HPT [18,29,47,48]. Recently, a study by AlMangour et al. [49] has introduced SPD on AM-fabricated 17-4 stainless steel by shot peening. This technique was able to improve the surface roughness, microhardness, yield strength, and wear resistance on the fabricated samples in which such improvements are associated with grain refinement down to sub-micron and nano-scale levels attained by shot peening. However, since shot peening is essentially a surface modification technique, i.e. the material used for shot peening only penetrates a short distance into the base structure, grain refinement, the nano-scale layer, hence the enhancement in the previously mentioned properties observed in the study mainly occur only at surface level. On the other hand, compared to shot peening, the strain-induced deformation in HPT process takes place throughout the disk rather than on surface only. Hence, the improvement in mechanical properties obtained by HPT, e.g. microhardness, yield and tensile strengths are expected to occur as a whole, i.e. on the bulk material and not only at selectively treated surfaces [50,51]. Furthermore, the shot-peened structure in that study

only yielded a microhardness value ~450 HV, which is lower than that obtained via HPT in this study, indicating that HPT processing could result in higher strength for AM-fabricated samples, compared to the shot peening treatment.

On the other hand, despite having excellent corrosion resistance, surface defects such as pores, cracks and surface roughness have been found to negatively influence the corrosion behaviour of 316L SS [52]. Various studies have reported poorer corrosion resistance in SLM-fabricated 316L SS samples compared to conventionally manufactured material independent of electrolyte environment due to the presence of pores in the solidified structure [26,45,53]. For example, Geenen et al. [45] found that corrosion attack on pores continues through the crevices, and in addition with cracks and oxides, further worsen the corrosion resistance of SLM-fabricated 316L SS in H_2SO_4 electrolyte. Sun et al. [53] observed preferential corrosion attack at the pre-existing pores inside SLM-fabricated 316L SS immersed in 0.9% NaCl solution due to the increasing aggressiveness of anolytes in the pores, resulting in breakdown in passivity and accelerated dissolution of metals.

In this study, appreciable porosity level was only obvious in the as-received SLM sample. Even though the porosity content is fairly small (0.679 ± 0.051 %), their uneven distribution throughout the sample significantly impacts the current density, corrosion rate and hence the corrosion performance of the as-received SLM 316L SS. Otero et al. [54] and Gabe [55] explained that the initially formed stable passive oxide layer becomes ruptured due to the attack by the Cl^- ions after the material is immersed inside the electrolyte, which then reaches the inside of the pores through the crevices formed due to the existence of active-passive cells between the insides of the pores and the interface of the material before the material disintegrates. The disintegration of metal in this study is confirmed by the EDX analysis (Table 5), in which a substantial decrease in Fe and Cr was observed at the pore area (Fig. 12(c)), accompanied by an increase in O content.

Apart from pores, the presence of inclusions and oxides were also considered as defects which contribute to pitting corrosion in stainless steel products. Studies have shown MnS inclusions could be nucleating sites for pits inside 316L SS [21,41]. This is because of the increased Cl^- ions concentration which preferentially attacks weak points (defects) on the surface of the material until the passive film at the weak points dissolves, forming pit holes [41]. This phenomenon was also found within the as-received SLM sample in this study as

shown in area F of Fig. 12(b) and Table 5, in which a slightly higher amount of Mn and the emergence of Cl element were present at the pit area. However, the corroded pits are scattered as the formation of inclusions is a random occurrence [26].

The combination of processing temperature, grain size, surface conditions (chemistry and defects), and corrosive media (environment) are found to influence the corrosion performance of 316L SS, hence it is difficult to isolate the effects of individual aspect on the corrosion resistance of the material [22,23]. Various studies have reported ambiguous results in the influence of grain size and corrosion medium on the corrosion performance of metals and alloys [36,42,56]. For example, Rifai et al. [57] observed an improvement in pitting potential and hence the pitting resistance when ultrafine-grained (UFG) Fe-20%Cr steel was produced via ECAP and exposed to 1000 mol m^{-3} NaCl solution. However, Nie et al. [37] observed a worse corrosion resistance in HPT-processed commercially pure Ti exposed to 3.5% NaCl solution after further grain refinements at higher HPT revolutions.

Hence, it is difficult to generalise the relationship between grain size and corrosion performance. However, Ralston and Birbilis [58] suggested that in general, the increase or decrease of corrosion resistance in a material due to grain refinement is dependent on the ability of the environment (corrosive media) to passivate. The corrosion resistance of a material is expected to decrease with grain refinement in active (non-passivating) media, e.g. HCl and H_2SO_4 solutions. Conversely, grain refinement would improve the corrosion resistance of a material when it is exposed to passive media, e.g. NaOH and NaCl solutions. However, in environments promoting active-passive response, grain refinement would accelerate uniform corrosion but reduces the susceptibility to localised corrosion.

The main mechanism of corrosion resistance improvement due to grain refinement in passivating environments is attributed to the enhanced formation and adhesion of passive films on the base metal as a result of increased grain boundary density [58]. Moreover, the higher strain-induced grain refinement obtained at higher HPT revolutions produces larger amounts of grain boundaries and non-equilibrium grain boundaries (or cell boundaries in this study), greater dislocation densities and higher residual stress on the samples, hence providing further nucleation sites for the passive oxide layers to become more stable and intact [36]. As a result, the improvement of corrosion resistance as the number of turns

increase could be attributed to the increased thickness and density of the passive oxide layer formed.

However, this pattern was no longer observed after 5 revolutions, as the corrosion rate increased before decreasing again after 10 turns. Overall, HPT processing has improved the corrosion resistance of SLM 316L SS. The best corrosion resistance as indicated by the corrosion rate values in Table 3 is obtained after 1 HPT revolution (0.41 ± 0.01 µm $year^{-1}$), followed closely by 10 turns (0.48 ± 0.21 µm $year^{-1}$). Despite 5 turns of HPT producing the worst corrosion rate among HPT-processed samples (2.14 ± 0.44 µm $year^{-1}$), it is still better than that of the as-received sample (2.53 ± 0.62 µm $year^{-1}$).

The unexpected deterioration in corrosion resistance after 5 turns could not possibly be attributed to the corrosion attack on the cell boundaries or even to pitting corrosion. This is because the attack on cell boundaries could no longer be observed beyond 1 HPT revolution, whereas the substantially greater E_{pit} value (1028 mV) obtained at 5 turns compared to the as-received sample and HPT-processed sample through lower number of turns (1/4, 1/2, and 1) indicates significantly enhanced resistance to pitting corrosion. Based on the SEM observations in Fig. 13, the lower corrosion rate obtained after 5 turns could be explained by the extent of crevice corrosion observed on the corroded sample. This observation is supported by EDX analysis shown in Table 6, in which the chromium content in the crevice was found to be the lowest among all HPT-processed samples. This indicates limited formation of passive Cr_2O_3 layer which promotes corrosion attack by aggressive Cl^- ions, resulting in a large and deep crevice [41].

However, the limitation of passive Cr_2O_3 layer formation at 5 turns of HPT processing could not be attributed to the cellular structure refinement alone because the higher cell boundary density obtained should in fact further encourage the formation of the passive oxide layers. Hence, this dichotomy could be explained by also considering the grain (or cells in this study) distribution throughout the fabricated samples, and not only in terms of grain (or cellular structure) refinement, as proposed by Gollapudi et al. [23]. They explained that in a passivating environment, for the same average grain size i.e. for a material having either fine or coarse grains only, a smaller distribution of grain size encourages improvement in corrosion resistance, and vice versa. On the other hand, for a bimodal microstructure i.e. having both fine and coarse grains simultaneously, in a passivating environment, corrosion

resistance is enhanced if the volume fraction of fine grains is higher than that of coarse grains, and vice versa [23].

Compared to the lower number of turns, the effect of extreme equivalent torsional strain imposed via HPT after 5 turns (Fig. 8(b)) indicate narrower cellular structure distribution (Fig. 6(d)), suggesting that some levels of re-distribution of dislocations and cellular structures or even grain boundary densities might happen within the cells and at the cell boundaries. This could significantly influence the cell or grain size distribution in the sample processed through 5 HPT revolutions, which weakens the capability to form passive oxide layer. Furthermore, further elemental segregations induced by the increasing torsional strains have also been found to cause spatially heterogeneous change in their compositions, which could alter the passivation mechanism of this material [22]. Hence, these suggest that the re-distribution of dislocation cells and eventually grains, as well as elemental segregation might influence the strain-induced surface reactivity such that it overpowers the formation of the passive oxide layers [58–60].

Nevertheless, except the samples processed through 5 HPT revolutions, the results from EIS (Table 4) show that the improvement in corrosion resistance within the HPT-processed samples is attributed to the formation of thicker and denser passive oxide layers as the number of turns increased. Based on the EC model of two layers in series which best fitted the experimental EIS data, the polarisation resistance, R_p is divided into R_{in} and R_{out}. R_{in} corresponds to impedance from the inner protective oxide layer, whereas R_{out} is related to that of the outside layer that contains pores or defects. Low R_{in} values mean that the passive oxide film formed on the inner layer is unstable when exposed to the electrolyte solution. On the other hand, low values of R_{out} are attributed to the presence of defects and pores on the outer surface layer.

Based on the results in Table 4, the low R_{out} value for the as-received SLM samples is expected due to the existence of appreciable amounts of pores on the outer surface. Similarly, the inner passive oxide layer formed after 1/4 turn outperforms the significant reduction in porosity level due to HPT processing as indicated by the higher R_{in} value compared to R_{out}, even though the value of R_{in} increased. After 1/4 HPT revolution, both the values of R_{in} and R_{out} increase significantly, which are indicative of thicker and denser passive oxide layers being formed. Some level of microstructural homogeneity has been achieved, and substantial

amounts of pores and surface defects have been eliminated. The significantly higher R_{out} values than R_{in} as the number of turns increased beyond 1/4 suggests that the considerable reduction of pores and defects due to HPT processing is much more effective in enhancing corrosion resistance, as compared to increasing active sites and improving microstructural homogeneity. However, within the HPT-processed samples, the reduction in R_{in} and R_{in} values after 5 HPT revolutions shows that the large crevices have negatively impacted the formation of passive oxide layers.

5. Conclusions

In this study, the novel combination of AM (SLM technique) and SPD (HPT process) has been studied together in a single process sequence. 316L SS was firstly fabricated by SLM and subsequently processed by HPT through 1/4, 1/2, 1, 5, and 10 turns, in which larger amounts of torsional strain was imposed on the samples as the number of HPT revolutions was increased.

The complex microstructures were observed with SEM and TEM in the SLM-fabricated sample with featuring 'island' scan tracks representing melt pools and cellular structures, which are attributed to the rapid heating and cooling cycle experienced during SLM. On the other hand, the torsional strain imposed during HPT introduced deformation in the scan tracks as well as in the cellular structures. The scan tracks were eliminated after 10 turns, while the cellular structures became increasingly elongated and narrower as the number of turns were increased. HPT processing has also successfully produce nano-scale grains after 10 turns.

It is also found that the application of large amounts of strain during HPT processing was able to effectively 'close' the pores and hence significantly reduce porosity content. In addition, the increase in microhardness values are attributed to the cellular structure refinement attained as the number of HPT revolutions increases.

Electrochemical testing performed in 3.5% NaCl solution demonstrated that HPT processing can generally improve the corrosion resistance of SLM 316L SS when compared with the as-received samples. However, within the HPT-processed samples, a noteworthy trend was observed that, as the number of turns increased from 1/4 to 1, the corrosion resistance

continuously improved, but deteriorated after 5 turns before improving again after 10 turns. Combined with SEM and EDX results, the observed enhancement in corrosion resistance of the HPT-processed SLM 316L SS is attributed to the significant pore reduction and microstructural homogeneity induced by HPT processing, as well as thereby increased thickness and density of the passive oxide layer formed on the processed sample surfaces.

Acknowledgements

This work was supported by a PhD studentship for S.M. Yusuf from Faculty of Engineering and the Environment at the University of Southampton, UK. Y. Chen would like to acknowledge the financial supports from the National Natural Science Foundation of China (No. 51601162) and High-Level Talent Funding for Xiamen Oversea Returnee.

References

[1] A. Riemer, S. Leuders, M. Thöne, H.A. Richard, T. Tröster, T. Niendorf, On the fatigue crack growth behavior in 316L stainless steel manufactured by selective laser melting, Eng. Fract. Mech. 120 (2014) 15–25. doi:10.1016/j.engfracmech.2014.03.008.

[2] B.E. Carroll, T.A. Palmer, A.M. Beese, Anisotropic tensile behavior of Ti-6Al-4V components fabricated with directed energy deposition additive manufacturing, Acta Mater. 87 (2015) 309–320. doi:10.1016/j.actamat.2014.12.054.

[3] B. Song, X. Zhao, S. Li, C. Han, Q. Wei, S. Wen, J. Liu, Y. Shi, Differences in microstructure and properties between selective laser melting and traditional manufacturing for fabrication of metal parts: A review, Front. Mech. Eng. 10 (2015) 111–125.

[4] S.M. Yusuf, N. Gao, Influence of energy density on metallurgy and properties in metal additive manufacturing, Mater. Sci. Technol. 33 (2017) 1269–1289. doi:10.1080/02670836.2017.1289444.

[5] M. Ma, Z. Wang, X. Zeng, A comparison on metallurgical behaviors of 316L stainless steel by selective laser melting and laser cladding deposition, Mater. Sci. Eng. A. 685 (2017) 265–273. doi:10.1016/j.msea.2016.12.112.

[6] J.J. Lewandowski, M. Seifi, Metal Additive Manufacturing: A Review of Mechanical Properties, Annu. Rev. Mater. Res. 46 (2016) 151–186. doi:10.1146/annurev-matsci-070115-032024.

[7] R.Z. Valiev, R.K. Islamgaliev, I. V. Alexandrov, Bulk nanostructured materials from severe plastic deformation, 2000. doi:10.1016/S0079-6425(99)00007-9.

[8] Y.T. Zhu, T.G. Langdon, The fundamentals of nanostructured materials processed by severe plastic deformation, J. Mater. 56 (2004) 58–63. doi:10.1007/s11837-004-0294-0.

[9] R.Z. Valiev, Y. Estrin, Z. Horita, T.G. Langdon, M.J. Zehetbauer, Y. Zhu, Producing Bulk Ultrafine-Grained Materials by Severe Plastic Deformation: Ten Years Later, J. Mater. 68 (2006) 1216–1226. doi:10.1007/s11837-016-1820-6.

[10] A.P. Zhilyaev, G. V. Nurislamova, B.K. Kim, M.D. Baró, J.A. Szpunar, T.G. Langdon, Experimental parameters influencing grain refinement and microstructural evolution during high-pressure torsion, Acta Mater. 51 (2003) 753–765. doi:10.1016/S1359-6454(02)00466-4.

[11] A.P. Zhilyaev, B.K. Kim, G. V. Nurislamova, M.D. Baró, J.A. Szpunar, T.G. Langdon, Orientation imaging microscopy of ultrafine-grained nickel, Scr. Mater. 46 (2002) 575–580. doi:10.1016/S1359-6462(02)00018-0.

[12] A.P. Zhilyaev, B.K. Kim, J.A. Szpunar, M.D. Baró, T.G. Langdon, The microstructural characteristics of ultrafine-grained nickel, Mater. Sci. Eng. A. 391 (2005) 377–389. doi:10.1016/j.msea.2004.09.030.

[13] J. Wongsa-Ngam, H. Wen, T.G. Langdon, Microstructural evolution in a Cu-Zr alloy processed by a combination of ECAP and HPT, Mater. Sci. Eng. A. 579 (2013) 126–135. doi:10.1016/j.msea.2013.05.010.

[14] J. Wongsa-Ngam, M. Kawasaki, T.G. Langdon, A comparison of microstructures and mechanical properties in a Cu-Zr alloy processed using different SPD techniques, J. Mater. Sci. 48 (2013) 4653–4660. doi:10.1007/s10853-012-7072-0.
[15] H. Yu, J. Yang, J. Yin, Z. Wang, X. Zeng, Comparison on mechanical anisotropies of selective laser melted Ti-6Al-4V alloy and 304 stainless steel, Mater. Sci. Eng. A. 695 (2017) 92–100. doi:10.1016/j.msea.2017.04.031.
[16] N. Read, W. Wang, K. Essa, M.M. Attallah, Selective laser melting of AlSi10Mg alloy: Process optimisation and mechanical properties development, Mater. Des. 65 (2015) 417–424. doi:10.1016/j.matdes.2014.09.044.
[17] K. Saeidi, X. Gao, F. Lofaj, L. Kvetková, Z.J. Shen, Transformation of austenite to duplex austenite-ferrite assembly in annealed stainless steel 316L consolidated by laser melting, J. Alloys Compd. 633 (2015) 463–469. doi:10.1016/j.jallcom.2015.01.249.
[18] J. Gubicza, M. El-Tahawy, Y. Huang, H. Choi, H. Choe, J.L. Lábár, T.G. Langdon, Microstructure, phase composition and hardness evolution in 316L stainless steel processed by high-pressure torsion, Mater. Sci. Eng. A. 657 (2016) 215–223. doi:10.1016/j.msea.2016.01.057.
[19] F.A. Mohamed, S.S. Dheda, On the minimum grain size obtainable by high-pressure torsion, Mater. Sci. Eng. A. 558 (2012) 59–63. doi:10.1016/j.msea.2012.07.066.
[20] C. Xu, Z. Horita, T.G. Langdon, The evolution of homogeneity in processing by high-pressure torsion, Acta Mater. 55 (2007) 203–212. doi:10.1016/j.actamat.2006.07.029.
[21] L. Gil, S. Brühl, L. Jiménez, O. Leon, R. Guevara, M.H. Staia, Corrosion performance of the plasma nitrided 316L stainless steel, Surf. Coatings Technol. 201 (2006) 4424–4429. doi:10.1016/j.surfcoat.2006.08.081.
[22] J.R. Trelewicz, G.P. Halada, O.K. Donaldson, G. Manogharan, Microstructure and Corrosion Resistance of Laser Additively Manufactured 316L Stainless Steel, Jom. 68 (2016) 850–859. doi:10.1007/s11837-016-1822-4.
[23] S. Gollapudi, Grain size distribution effects on the corrosion behaviour of materials, Corros. Sci. 62 (2012) 90–94. doi:10.1016/j.corsci.2012.04.040.
[24] A. Di Schino, J.M.J. Kenny, Effects of the grain size on the corrosion behavior of refined AISI 304 austenitic stainless steels, J. Mater. Sci. Lett. 21 (2002) 1631–1634. doi:10.1023/A:1020338103964.
[25] Y. Li, F. Wang, Grain size effect on the electrochemical corrosion behavior of surface nanocrystallized low-carbon steel, Corrosion. 60 (2004) 891–896. http://cat.inist.fr/?aModele=afficheN&cpsidt=16173587.
[26] G. Sander, S. Thomas, V. Cruz, M. Jurg, N. Birbilis, X. Gao, M. Brameld, C.R. Hutchinson, On The Corrosion and Metastable Pitting Characteristics of 316L Stainless Steel Produced by Selective Laser Melting, J. Electrochem. Soc. 164 (2017) C250–C257. doi:10.1149/2.0551706jes.
[27] R.B. Figueiredo, P.R. Cetlin, T.G. Langdon, Using finite element modeling to examine the flow processes in quasi-constrained high-pressure torsion, Mater. Sci. Eng. A. 528 (2011) 8198–8204. doi:10.1016/j.msea.2011.07.040.
[28] a. Thorvaldsen, The intercept method—1. Evaluation of grain shape, Acta Mater. 45 (1997) 587–594. doi:10.1016/S1359-6454(96)00197-8.
[29] Y. Zhong, L. Liu, S. Wikman, D. Cui, Z. Shen, Intragranular cellular segregation network structure strengthening 316L stainless steel prepared by selective laser melting, J. Nucl. Mater. 470 (2016) 170–178. doi:10.1016/j.jnucmat.2015.12.034.
[30] Z. Sun, X. Tan, S.B. Tor, W.Y. Yeong, Selective laser melting of stainless steel 316L with low porosity and high build rates, Mater. Des. 104 (2016) 197–204. doi:10.1016/j.matdes.2016.05.035.
[31] M. Ziętala, T. Durejko, M. Polański, I. Kunce, T. Płociński, W. Zieliński, M. Łazińska, W. Stępniowski, T. Czujko, K.J. Kurzydłowski, Z. Bojar, The microstructure, mechanical properties and corrosion resistance of 316L stainless steel fabricated using laser engineered net shaping, Mater. Sci. Eng. A. 677 (2016) 1–10. doi:10.1016/j.msea.2016.09.028.
[32] A. Loucif, R.B. Figueiredo, T. Baudin, F. Brisset, T.G. Langdon, Microstructural evolution in an Al-6061 alloy processed by high-pressure torsion, Mater. Sci. Eng. A. 527 (2010) 4864–4869. doi:10.1016/j.msea.2010.04.027.
[33] M.I.A. El Aal, H.S. Kim, Wear properties of high pressure torsion processed ultrafine grained Al-7%Si alloy, Mater. Des. 53 (2014) 373–382. doi:10.1016/j.matdes.2013.07.045.
[34] C.T. Wang, N. Gao, M.G. Gee, R.J.K. Wood, T.G. Langdon, Effect of grain size on the micro-tribological behavior of pure titanium processed by high-pressure torsion, Wear. 280–281 (2012) 28–35. doi:10.1016/j.wear.2012.01.012.
[35] ASTM, ASTM G 102-89: Standard Practice for Calculation of Corrosion Rates and Related Information, 1999. doi:10.1520/G0102-89R10.
[36] X. Wang, M. Nie, C.T. Wang, S.C. Wang, N. Gao, Microhardness and corrosion properties of

hypoeutectic Al-7Si alloy processed by high-pressure torsion, Mater. Des. 83 (2015) 193–202. doi:10.1016/j.matdes.2015.06.018.
[37] M. Nie, C.T. Wang, M. Qu, N. Gao, J.A. Wharton, T.G. Langdon, The corrosion behaviour of commercial purity titanium processed by high-pressure torsion, J. Mater. Sci. 49 (2014) 2824–2831. doi:10.1007/s10853-013-7988-z.
[38] A. Norlin, J. Pan, C. Leygraf, Investigation of interfacial capacitance of Pt, Ti and TiN coated electrodes by electrochemical impedance spectroscopy, Biomol. Eng. 19 (2002) 67–71. doi:10.1016/S1389-0344(02)00013-8.
[39] A. Szummer, M. Janik-Czachor, S. Hofmann, Discontinuity of the passivating film at nonmetallic stainless steels, Mater. Sci. Commun. 34 (1993) 181–183.
[40] D.E. Williams, T.F. Mohiuddin, Y.Y. Zhu, Elucidation of a trigger mechanism for pitting corrosion of stainless steels using submicron resolution scanning electrochemical and photoelectrochemical microscopy, J. Electrochem. Soc. 145 (1998) 2664–2672. doi:10.1149/1.1838697.
[41] J.X. Zou, K.M. Zhang, S.Z. Hao, C. Dong, T. Grosdidier, Mechanisms of hardening, wear and corrosion improvement of 316 L stainless steel by low energy high current pulsed electron beam surface treatment, Thin Solid Films. 519 (2010) 1404–1415. doi:10.1016/j.tsf.2010.09.022.
[42] S. Tamilselvi, R. Murugaraj, N. Rajendran, Electrochemical impedance spectroscopic studies of titanium and its alloys in saline medium, Mater. Corros. 58 (2007) 113–120. doi:10.1002/maco.200603979.
[43] S.L. De Assis, S. Wolynec, I. Costa, Corrosion characterization of titanium alloys by electrochemical techniques, Electrochim. Acta. 51 (2006) 1815–1819. doi:10.1016/j.electacta.2005.02.121.
[44] J.-B. Jorcin, M.E. Orazem, N. Pébère, B. Tribollet, CPE analysis by local electrochemical impedance spectroscopy, Electrochim. Acta. 51 (2006) 1473–1479. doi:10.1016/j.electacta.2005.02.128.
[45] K. Geenen, A. Röttger, W. Theisen, Corrosion behavior of 316L austenitic steel processed by selective laser melting, hot-isostatic pressing, and casting, Mater. Corros. 9999 (2017) 1–12. doi:10.1002/maco.201609210.
[46] K. Sasaki, G.T. Burstein, The generation of surface roughness during slurry erosion-corrosion and its effect on the pitting potential, Corros. Sci. 38 (1996) 2111–2120. doi:10.1016/S0010-938X(96)00066-2.
[47] K. Saeidi, X. Gao, Y. Zhong, Z.J. Shen, Hardened austenite steel with columnar sub-grain structure formed by laser melting, Mater. Sci. Eng. A. 625 (2015) 221–229. doi:10.1016/j.msea.2014.12.018.
[48] S. Yusuf, Y. Chen, R. Boardman, S. Yang, N. Gao, Investigation on Porosity and Microhardness of 316L Stainless Steel Fabricated by Selective Laser Melting, Metals (Basel). 7 (2017) 1–12. doi:10.3390/met7020064.
[49] B. AlMangour, J.M. Yang, Improving the surface quality and mechanical properties by shot-peening of 17-4 stainless steel fabricated by additive manufacturing, Mater. Des. 110 (2016) 914–924. doi:10.1016/j.matdes.2016.08.037.
[50] K. Edalati, Z. Horita, A review on high-pressure torsion (HPT) from 1935 to 1988, Mater. Sci. Eng. A. 652 (2016) 325–352. doi:10.1016/j.msea.2015.11.074.
[51] L.S. Toth, C. Gu, Ultrafine-grain metals by severe plastic deformation, Mater. Charact. 92 (2014) 1–14. doi:10.1016/j.matchar.2014.02.003.
[52] A. Röttger, K. Geenen, M. Windmann, F. Binner, W. Theisen, Comparison of microstructure and mechanical properties of 316 L austenitic steel processed by selective laser melting with hot-isostatic pressed and cast material, Mater. Sci. Eng. A. 678 (2016) 365–376. doi:10.1016/j.msea.2016.10.012.
[53] Y. Sun, A. Moroz, K. Alrbaey, Sliding wear characteristics and corrosion behaviour of selective laser melted 316L stainless steel, J. Mater. Eng. Perform. 23 (2014) 518–526. doi:10.1007/s11665-013-0784-8.
[54] E. Otero, A. Pardo, M. V. Utrilla, E. Sáenz, J.F. Álvarez, Corrosion behaviour of AISI 304L and 316L stainless steels prepared by powder metallurgy in the presence of sulphuric and phosphoric acid, Corros. Sci. 40 (1998) 1421–1434. doi:10.1016/S0010-938X(98)00047-X.
[55] D.R. Gabe, Corrosion and Protection of Sintered Metal Parts, Powder Metall. 20 (1977) 227–231. doi:10.1179/pom.1977.20.4.227.
[56] Y. Liu, D. Liu, C. You, M. Chen, Effects of grain size on the corrosion resistance of pure magnesium by cooling rate-controlled solidification, Front. Mater. Sci. 9 (2015) 247–253. doi:10.1007/s11706-015-0299-3.
[57] M. Rifai, H. Miyamoto, H. Fujiwara, Effects of Strain Energy and Grain Size on Corrosion Resistance of Ultrafine Grained Fe-20 % Cr Steels with Extremely low C and N Fabricated by ECAP, Int. J. Corros. 2015 (2015) 1–9.
[58] K.D. Ralston, N. Birbilis, Effect of grain size on corrosion, Corrosion. 66 (2010) 1–4. doi:10.5006/1.3462912.
[59] E. Akiyama, Z. Zhang, Y. Watanabe, K. Tsuzaki, Effects of severe plastic deformation on the corrosion

behavior of aluminum alloys, J. Solid State Electrochem. 13 (2009) 277–282. doi:10.1007/s10008-007-0496-9.

[60] D. Song, A. Ma, J. Jiang, P. Lin, D. Yang, Corrosion behavior of ultra-fine grained industrial pure Al fabricated by ECAP, Trans. Nonferrous Met. Soc. China (English Ed. 19 (2009) 1065–1070. doi:10.1016/S1003-6326(08)60407-0.

Highlights

Title: Microstructure and corrosion performance of 316L stainless steel fabricated by Selective Laser Melting and processed through High-pressure Torsion

Authors: Shahir Mohd Yusuf, Mengyan Nie, Ying Chen, Shoufeng Yang and Nong Gao*

Highlights:

- Additive manufacturing and High-pressure Torsion (HPT) are combined for the first time.
- Novel microstructures with grain refinement down to nanometer scale are obtained.
- Significant pore reduction and remarkable increase in microhardness are observed.
- Enhancement of corrosion performance in 3.5% NaCl solution is achieved via HPT.